AIAA JOURNAL
Vol. 48, No. 8, August 2010

Turbulent Boundary-Layer Separation Control with Single Dielectric Barrier Discharge Plasma Actuators

David M. Schatzman* and Flint O. Thomas†
University of Notre Dame, Notre Dame, Indiana 46637

DOI: 10.2514/1.J050009

An experimental study was conducted to determine the effect of single dielectric barrier discharge plasma actuators on turbulent boundary-layer separation control. Two-component particle image velocimetry and laser Doppler velocimetry measurements showed the effect of plasma actuators on ambient air, a canonical zero-pressure gradient turbulent boundary layer, and a two-dimensional turbulent boundary-layer separation from a convex ramp section. Different actuator configurations and control strategies were implemented. Spanwise actuators were operated in both steady and unsteady modes. Plasma streamwise vortex generators were also used to enhance boundary-layer mixing. Flow visualization using a high-speed camera captured the temporal aspects of the separation control process and helped discern the physical mechanisms associated with each actuation strategy. The steady spanwise actuation produced a wall jet effect that augmented near-wall momentum and reattached the separated boundary layer. The streamwise oriented actuators also showed effective control authority by creating counter-rotating vortices within the boundary layer that promote mixing of high and low momentum fluid.

Nomenclature

b	=	covered electrode width
C_p	=	pressure coefficient
f	=	unsteady actuation frequency
H	=	shape factor
h	=	dielectric thickness
L	=	length of ramp section
Re_x	=	Reynolds number
U_∞	=	freestream velocity
x	=	streamwise distance along ramp section
x_p	=	streamwise distance along boundary-layer development plate
z	=	exposed electrode spacing
δ	=	boundary-layer thickness
δ^*	=	displacement thickness
ε	=	dielectric coefficient
θ	=	momentum thickness
θ_x	=	local ramp curvature angle

I. Introduction

IN THIS paper single dielectric barrier discharge (SDBD) plasma actuators are used to control turbulent boundary-layer separation from a two-dimensional convex ramp. The two-dimensional convex ramp is a fundamental experimental configuration that is analogous to flows of practical significance such as the flow over a deflected aft control surface on a wing, an upswept aircraft fuselage, and the aft portion of a sedan automobile.

There is a considerable body of literature dealing with boundary-layer separation control by both passive and active means [1]. The importance of exploiting unsteady mechanisms in active control schemes is widely recognized [2]. Active separation control methods currently receiving considerable attention are synthetic jet actuators [3,4] and dielectric barrier discharge (DBD) plasma actuators [5]. This study is focused upon active control of turbulent boundary-layer separation using DBD plasma actuators. Most of the previous work using plasma actuators has focused on separation control of thin laminar boundary layers such as leading-edge separation control [6], control of dynamic stall on oscillating airfoils [7], and control of subcritical separation and vortex shedding from a cylinder in crossflow [8–10]. The work presented here is motivated by the need to use plasma actuators for flow control of turbulent boundary-layer separation that occurs in high Reynolds number aerodynamic flows.

The basic physics of the plasma actuator is described by Enloe et al. [11,12]. The SDBD plasma actuator consists of an asymmetric arrangement of two electrodes separated by dielectric barrier material as shown schematically in Fig. 1. Some of the materials with suitable dielectric properties include Kapton, Macor, quartz, and Teflon. The exposed electrode and the insulated electrode generally have a small amount $\mathcal{O}$(mm) of overlap to provide a sufficiently large local electric field. A high voltage $\mathcal{O}$(kV) a.c. input is supplied to the electrodes. When the amplitude of the a.c. input is large enough, the air will locally ionize in the region of the largest electric field. This generally occurs at the edge of the exposed electrode. The ionized air, in the presence of the electric field, produces a body force on the ambient air.

The asymmetric arrangement of the electrodes results in a strongly asymmetric body force. The body force draws ambient air toward the wall, and the impermeability of the wall induces a two-dimensional wall jet, which should be useful in maintaining attached boundary-layer flow. In addition to the wall jet, Post [13] demonstrated electrode arrangements that could produce spanwise and streamwise vortices in a boundary layer. He and Corke [14] demonstrated the use of plasma streamwise vortex generators (PSVG) to control a canonical turbulent separated flow on a wall mounted hump model.

Corke et al. [5] and Moreau [15] provide comprehensive reviews of the physics, design, and flow control applications of SDBD plasma actuators. Forte et al. [16] performed an optimization study of plasma actuator design based on measurements of the plasma-induced velocity. Thomas et al. [17] investigated the effect of the dielectric material and thickness on the induced thrust from a SDBD actuator. Design of actuators using thicker dielectric materials resulted in an order of magnitude improvement of the actuator-induced thrust (proportional to body force) as compared with the typical Kapton film-based actuator. It was shown that dielectric materials with a low dielectric constant and increased thickness allow for higher sustainable applied a.c. voltage without arcing or entering the

Presented as Paper 2008-4199 at the 4th AIAA Flow Control Conference Seattle, WA, 23–26 June 2008. Received 17 June 2009; revision received 13 January 2010; accepted for publication 25 January 2010.

*Graduate Research Assistant, Department of Aerospace and Mechanical Engineering. Member AIAA.

†Professor, Department of Aerospace and Mechanical Engineering. Associate Fellow AIAA.

filamentary regime of the plasma. The ability to form a uniform glow discharge at higher voltages results in an increase in the maximum achievable body force (i.e., thrust).

Plasma actuators can be used in either steady or unsteady operation. Although an a.c. voltage is required for operation of DBD plasma actuators, if the frequency is much higher than the characteristic frequency associated with the flowfield then the actuation is effectively quasi-steady. Typical plasma carrier frequencies range from 1 to 10 kHz. The optimum carrier frequency depends on the bulk capacitance of the dielectric material [18], which is proportional to ε/h, where ε is the dielectric coefficient, and h is the thickness of the dielectric material. Unsteady actuation involves turning the actuator on and off during each unsteady actuation period. Unsteady actuation requires less power than steady actuation for the same input voltage due to the reduced duty cycle. In addition, measurements have shown that the mechanism of flow control is quite different for steady and unsteady operation of the actuators [10,19–22].

In contrast with the plasma actuator with spanwise-oriented electrodes shown in Fig. 1, a schematic illustration of the plasma streamwise vortex generator (PSVG) is shown in Fig. 2. This configuration uses a single covered electrode with width, b, and is separated from the exposed electrodes by a dielectric barrier material. The multiple exposed electrodes with spacing z are aligned parallel to the oncoming flow. Instead of a wall jet, the PSVG arrangement is designed to generate pairs of counter-rotating vortices with size $\mathcal{O}(z/2)$. These are intended to enhance the cross-stream mixing within the boundary layer for separation control.

The objective of this paper is to both demonstrate and discern the physical mechanism(s) associated with turbulent boundary-layer separation control using SDBD plasma actuation. Actuators featuring spanwise-oriented electrodes as well as PSVGs are used, and their effect is compared. This is accomplished through boundary-layer measurements and flow visualization with high spatial and temporal resolution. Measurements demonstrate the induced flow of both types of plasma actuators in still air and the effect the actuator-induced flow has on a canonical flat plate zero pressure gradient (ZPG) turbulent boundary-layer flow. The results are subsequently applied to the control of adverse pressure gradient (APG) turbulent boundary-layer separation from a two-dimensional convex ramp section.

II. Experimental Setup

A. Turbulent Boundary-Layer Separation Model

The experiments are conducted in a subsonic open-return wind tunnel in the Hessert Laboratory at the University of Notre Dame. The wind tunnel has an inlet with a contraction ratio of 20:1. The inlet has a series of 12 turbulence management screens to condition the flow resulting in freestream turbulence levels of less than 0.1% for frequencies greater than 10 Hz. Air is drawn through the inlet by an eight-bladed fan connected to an 18.6 kW a.c. induction motor. The test section is 0.610 m × 0.610 m in cross section and 1.83 m in length. One test section side wall and a window in the test section ceiling are made from glass to provide optical access to the flowfield.

The test section model consists of a flat boundary-layer development plate followed by a convex ramp of constant curvature at the plate trailing edge. A schematic of the model that spans the 0.610 m test section is shown in Fig. 3. A smooth s-shaped contour, constructed from sheet metal, brings the flow from the floor of the wind-tunnel inlet up to the level of the flat boundary-layer development plate. At the transition of the contour and flat plate, the boundary layer is tripped with a 5.08 cm wide strip of distributed sand grain roughness. The boundary-layer development plate is 0.914 m in length. The ramp geometry consists of 5° inserts that connect together to create a hydrodynamically smooth constant radius arc of 0.510 m. The results presented in this paper are for a fixed ramp angle of 25° (defined in Fig. 3). Following the ramp curvature, a 0.152 m flat plate is installed to extend the length of the ramp section. A fairing, constructed from Teflon sheeting, smoothly transitions the end of the ramp to the floor of the test section.

Measurements were first conducted to characterize the turbulent boundary-layer flow over the model and to document the two-dimensional ramp separation characteristics. Boundary-layer measurements on the plate upstream of the ramp section were conducted

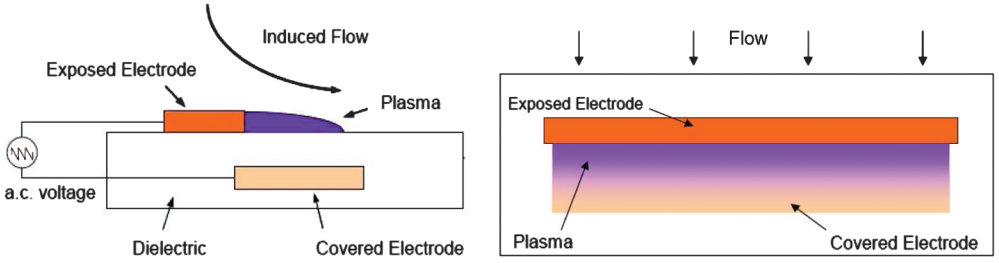

a) b)

Fig. 1 Schematic of the SDBD spanwise-oriented plasma actuator: a) side view, and b) top view.

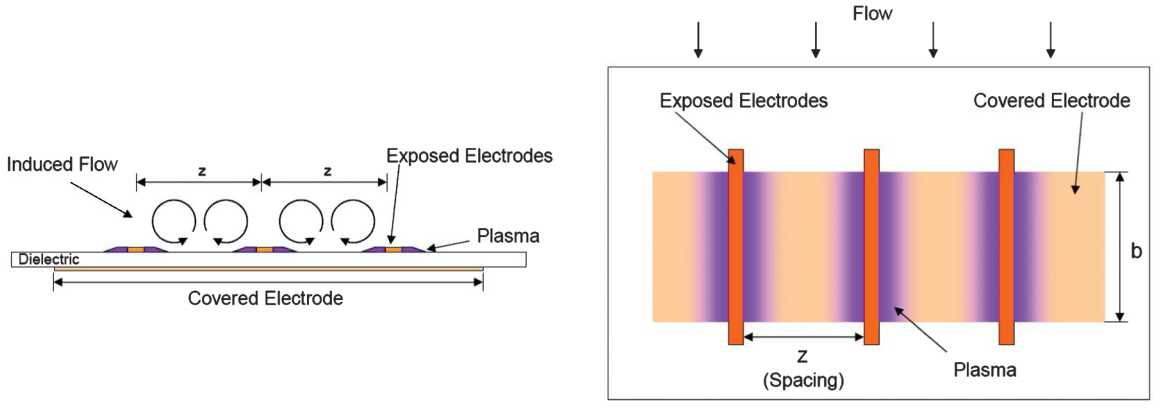

a) b)

Fig. 2 Schematic illustration of PSVG actuator: a) rear view, and b) top view.

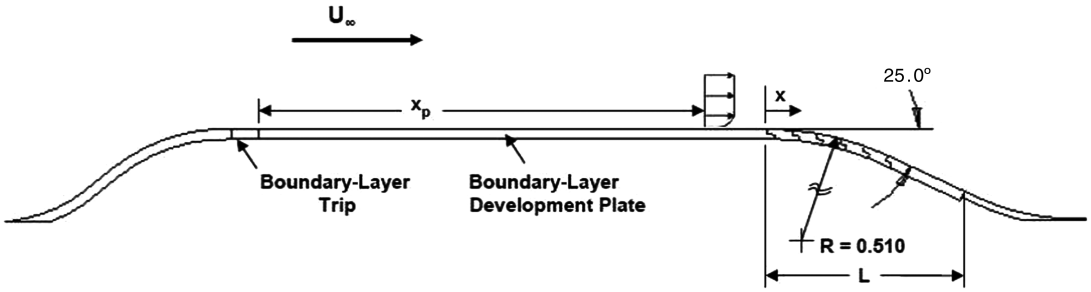

Fig. 3 Schematic of the turbulent boundary-layer development plate and convex ramp section.

using constant temperature hot-wire anemometry. The measurements were conducted at $x_p = 0.883$ m, where x_p is the streamwise distance along the boundary development plate as measured from the boundary-layer trip. The boundary-layer mean velocity profiles shown in Fig. 4a collapse to the typical ZPG turbulent boundary-layer profile [23] for the range of Reynolds numbers tested ($Re_\theta = 820$–3500). The boundary-layer mean velocity profiles plotted using inner variable scaling in Fig. 4b show that the flow approaching the ramp section exhibits the classic log-law behavior of a canonical ZPG turbulent boundary layer.

An evenly spaced distribution of 34 pressure taps were drilled along the spanwise centerline of the ramp section. The pressure taps were connected to a 48 port Scanivalve SSS-48C9 system, which houses a differential pressure transducer (model number PDCR23D) with a range of 10 in. of water. The surface pressure coefficient C_p is defined as

$$C_p = (p - p_\infty)/(p_0 - p_\infty) \tag{1}$$

where p is the static pressure measured at a given wall pressure tap, p_0 and p_∞ are the total and static pressures, respectively, as measured by a Pitot-static probe mounted from the wind-tunnel ceiling 32 mm upstream of the ramp section. The measured C_p values have $\pm 2.8\%$ relative uncertainty. Figure 5 shows the surface pressure distribution over the ramp section. The C_p distribution is plotted as a function of x/L, where x is the streamwise distance along the ramp surface and L is the total length of the ramp. The results show that after an initial favorable pressure gradient over the first ramp insert, there is a large adverse pressure gradient over the curvature of the ramp. The C_p values then level off to a constant value indicating a region of fully separated flow.

Oil flow surface visualization was conducted to determine the global separation characteristics on the ramp as a result of the imposed adverse pressure gradient. A thin layer of a mixture of 10W-40 oil and titanium dioxide was painted on the ramp surface. The wind tunnel was brought up to speed and the oil flow pattern was allowed to reach its steady state and then photographed. A sample image of oil flow surface visualization over the 25° ramp section is shown in Fig. 6a. At $x/L = 0.67$ the flow completely separates off the surface of the ramp. Although the surface oil flow pattern shows a fine-scale 3-D structure, the separation line is actually remarkably uniform in the spanwise direction, with the only significant deviation occurring near the side walls of the test section. This indicates a well-defined, two-dimensional flow separation in the mean. Further, the flow control measurements to be presented were confined to locations near the spanwise centerplane of the ramp. Pulsed Nd:Yag laser light sheet smoke visualization in the spanwise centerplane of the two-dimensional ramp section shown in Fig. 6b exhibits separation of the boundary layer from the ramp surface.

B. Plasma Actuation

The dielectric used for actuator construction was 1/8 inch thick Virgin Electrical Grade PTFE Teflon sheets with each side covered by a layer of 2 mil Kapton film and a layer of 2 mil Teflon tape. The flush mounted Teflon sheet was contoured to fit the local curvature of the ramp section and was held in place by nylon screws. Figure 7 shows installation locations of the Teflon dielectric for actuators on both the boundary-layer development plate and the ramp section. Each plasma actuator electrode consisted of 0.05 mm thick copper foil tape. The covered electrode was 356 mm in length and 51 mm wide. For the spanwise actuator the exposed electrode was 16 mm wide and 381 mm in length, which covers 62.5% of the test section span. For the PSVG actuators, each exposed electrode was 3 mm wide. For the spanwise actuator the electrodes had an overlap of approximately 2 mm to ensure uniform plasma in the spanwise direction. For flow control over the ramp section, the actuators were located upstream of the separation location at $\theta_x = 18°$, where θ_x is the local ramp curvature angle for the 25° ramp section. The location for the spanwise actuator was defined by the downstream edge of the

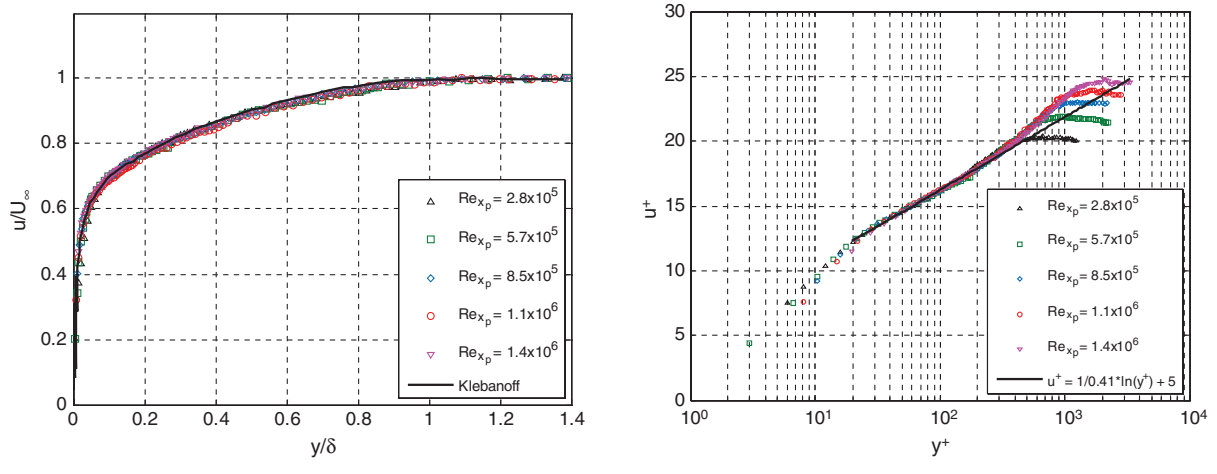

a) b)

Fig. 4 Boundary-layer measurements over flat development plate: a) mean velocity profiles in outer variable scaling, and b) mean velocity distribution with inner variable scaling.

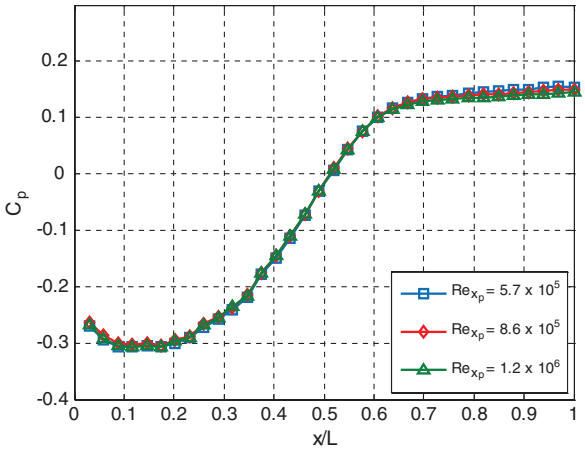

Fig. 5 Surface pressure distribution over the 25° ramp section.

exposed electrode. The location for the PSVG actuator was defined by the upstream edges of the exposed electrodes. Schematic illustrations of the actuator layout are shown in Fig. 8 for the spanwise actuator (part a) and the PSVG actuator (part b). The plasma generation circuit used to create the high-frequency, high-amplitude a.c. signal supplied to the actuator is described in detail by Schatzman et al. [24].

III. Results

A. Plasma Actuation Without External Flow

Before attempting boundary-layer flow control, the global velocity field induced by the actuators in the absence of external flow was measured using two-component particle image velocimetry (PIV). With both ends of the test section sealed, the air inside was seeded using olive oil droplets of nominally 1 μm diameter produced by a TSI atomizer. A model Y120-15 New Wave Research Nd:Yag laser system was positioned on top of the test section and provided a light sheet through the glass window to the centerplane of the actuator mounted on the flat plate. The laser produced double pulses with a 25 μs interval at a maximum repetition rate of 15 Hz. PIV images were captured by a PIV CAM 10-30 digital camera. TSI Insight 6 software was used to process the image pairs and compute the velocity fields. The measurement uncertainty for the velocity vectors is estimated to be within 2.0%, and the vorticity within 10%.

Figure 9 shows the mean velocity field from an ensemble average of 200 image pairs induced by a single spanwise-oriented actuator operated in steady mode by using a sawtooth waveform with a carrier frequency of 2 kHz. The measurement captures the fundamental features of the plasma actuator, in which ambient air is drawn downward toward the edge of the exposed electrode and results in the formation of a wall jet in the direction of the downstream edge of the

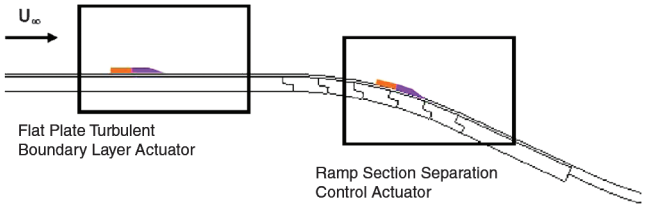

Fig. 7 Schematic of boundary-layer development plate and ramp section with Teflon dielectric installed for plasma actuation.

covered electrode. Figure 10 shows the induced mean velocity field for the case of unsteady actuation at $f = 20$ Hz with a duty cycle of 40%. The unsteady actuation results in a wider velocity profile due to the formation of spanwise vortices at the unsteady actuation frequency. These travel downstream and away from the wall. As such, it is expected that the physics of plasma flow control will be quite different for steady and unsteady actuation.

Measurements of the actuator-induced wall-normal velocity profiles downstream of the actuator were conducted using a Dantec Dynamics Fiber Flow laser Doppler velocimetry (LDV) system with a Spectra Physics Stabilite 2017 Argon-Ion Laser. The LDV system allows better near-wall resolution of the velocity field than PIV. The fiber optic LDV system was operated in 180° backscatter mode. The Doppler bursts were measured using a BSA F60 Flow processor and BSA Flow Software Version 4.10. To obtain measurements near the wall, only the horizontal component of the 2D 60 mm probe was used. The fiber optic probe was traversed normal to the surface of the flat plate for measurements of the induced velocity profiles for the different actuation strategies. The LDV mean velocity measurements have ±3.3% relative uncertainty.

The mean and rms velocity profiles measured 75 mm downstream of the exposed electrode of the spanwise actuator for both steady and unsteady actuation are shown in Fig. 11a and 11b. The mean profiles show wall jet characteristics for steady actuation and wider profiles due to unsteady actuation. The wall jet maximum velocity increases with increased applied voltage for steady actuation, and the unsteady actuation maximum velocity increases with the increased duty cycle. The maximum values of the rms velocity profiles for steady actuation correspond to the inflection points of the wall jet mean velocity profile. For unsteady actuation the rms velocity profiles show a second peak away from the wall that is due to the formation of spanwise vortices at the unsteady actuation frequency. Because there is no phase reference for the steady actuation cases, no distinction has been made between coherent perturbations and random fluctuations for the unsteady actuation rms velocity profiles.

PIV measurements of the actuator-induced global flowfield were repeated for the PSVG actuator configuration. The PIV laser plane was aligned over the exposed electrodes, resulting in a measurement plane similar to that illustrated in Fig. 2a. The induced velocity fields of the PSVG configuration for $V_{pp} = 35$ kV are shown in Figs. 12a and 12b for electrode spacings of 25 and 38 mm, respectively. The

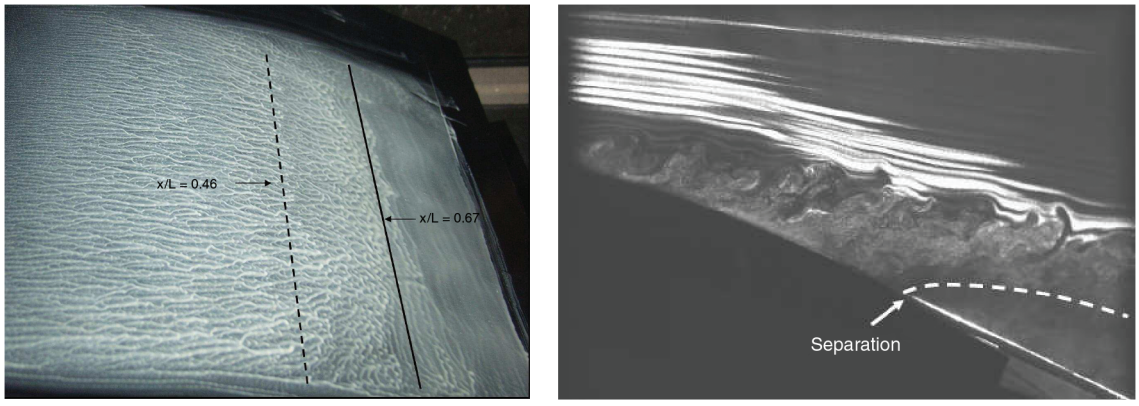

a) b)

Fig. 6 Flow visualization on ramp section with flow from left to right for a) oil surface visualization, and b) smoke visualization.

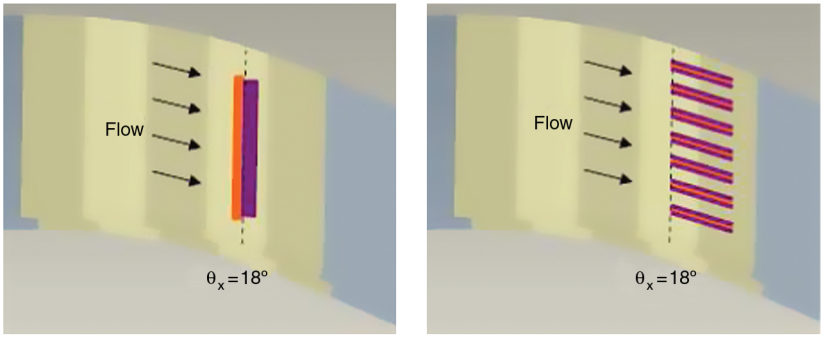

a) b)

Fig. 8 Schematic illustration of plasma formation on ramp section for a) spanwise actuator, and b) PSVG.

corresponding streamwise-component vorticity fields are shown in Fig. 13. The measurements show a downward induced velocity toward the edge of each exposed electrode. The flow is jetted away from each edge of the exposed electrodes and along the dielectric surface. Pairs of opposed wall jets collide and result in a strong upward induced velocity centered between two exposed electrodes. The magnitude of the induced velocity field increases with increasing voltage.

The larger spacing results in a stronger upward induced velocity field when compared with the lower spacing. Increasing the spacing between the exposed electrodes results in effectively increasing the relative area of the dielectric surface for the exposed electrode to deposit charge. This is similar to increasing the covered electrode width of a spanwise actuator, which has been shown to increase the plasma induced velocity for a fixed voltage [11]. The lower spacing results in a higher concentration of streamwise vorticity in the near-wall region throughout the span of the actuator. The regions of counter-rotating vorticity are separated by a distance of approximately $z/2$.

B. Flat Plate Boundary-Layer Actuation

The effect of spanwise plasma actuation on the ZPG turbulent boundary layer over the flat plate was measured nonintrusively using the LDV system. The actuator was placed such that the downstream edge of the exposed electrode was 0.762 m from the boundary-layer trip at the leading edge of the development plate. The results presented here were conducted at a freestream velocity of 5 m/s ($Re_x = 2.8 \times 10^5$). This freestream velocity was selected to demonstrate the effect of plasma actuation for the applied voltage range and for flow visualization clarity. It certainly should not be interpreted as an upper velocity limit for effective plasma control. It may be noted that in proprietary experiments on a full airframe configuration we have demonstrated DBD plasma drag reduction at tunnel speeds in excess of 100 m/s using actuators with thick dielectric barrier [17].

The turbulent boundary-layer velocity profiles measured 75 mm downstream ($\Delta x/\delta = 3.7$) of the spanwise actuator are shown in Fig. 14. The mean velocity profile measured with the LDV system for the baseline flow over the actuator compares well with the hot-wire measurements shown previously in Fig. 4a. The LDV measurements of u/U_∞ have $\pm 3.4\%$ relative uncertainty. The profiles for steady actuation in Fig. 14a show characteristics of near-wall momentum addition through a steady wall jet. The effect on the boundary-layer mean velocity profile increases with applied voltage. Steady actuation at 40 kV reduced the 99% boundary-layer thickness by 5.1% when compared with the plasma-off case. The momentum thickness and displacement thickness were reduced by 57 and 58%, respectively. This resulted in a velocity profile shape factor, $H \equiv \delta^*/\theta$, with a similar value as the plasma-off case, $H = 1.51$.

For the case of unsteady actuation at $f = 20$ Hz (a frequency that is $\mathcal{O}(0.1U_\infty/\delta)$, shown in Fig. 14b, the velocity profiles show momentum addition as a result of unsteady forcing. Unsteady actuation at 30 kV and 40% duty cycle resulted in a similar boundary-layer profile as the unsteady actuation case of 40 kV and 20% duty cycle. Hence, near-wall momentum addition can be increased by increasing either the duty cycle or the applied voltage. For unsteady actuation at 40 kV and 40% duty cycle, the 99% boundary-layer thickness was reduced by 2.1%. The momentum thickness and displacement thickness were both reduced by 26%, resulting in a shape factor with the same value as the plasma-off case, $H = 1.50$.

The corresponding streamwise-component turbulence intensity profiles for spanwise actuation of the flat plate turbulent boundary layer are shown in Fig. 15. The LDV measurements for turbulence intensity have $\pm 3.5\%$ relative uncertainty. Steady actuation reduced the turbulence intensity throughout 60% of the boundary-layer thickness as shown in Fig. 15a. The unsteady actuation results in Fig. 15b showed an increase in turbulence intensity for 30% of the boundary-layer thickness. This is attributed to the injection of spanwise vorticity into the boundary layer.

The boundary-layer characteristics for the flat plate turbulent boundary-layer actuation cases are summarized in Table 1. The table clearly shows that although the plasma actuation has a minimal effect on the boundary-layer thickness, there are large reductions in integral displacement and momentum thickness. This should prove beneficial for preventing flow separation in APG boundary-layer flows.

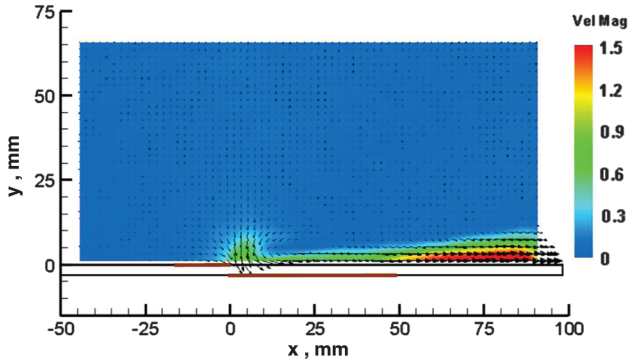

Fig. 9 Induced velocity field in ambient air for spanwise steady actuation at $V_{pp} = 40$ kV.

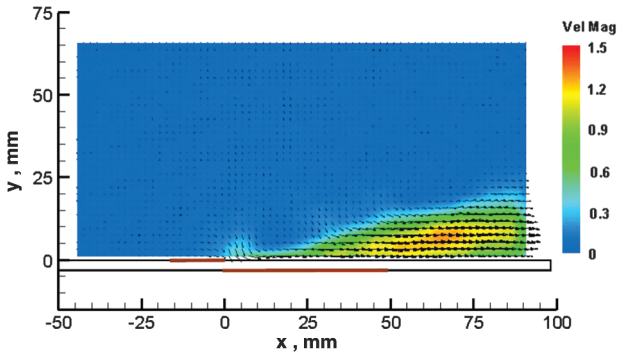

Fig. 10 Induced velocity field in ambient air for spanwise unsteady actuation at $V_{pp} = 40$ kV and 40% duty cycle.

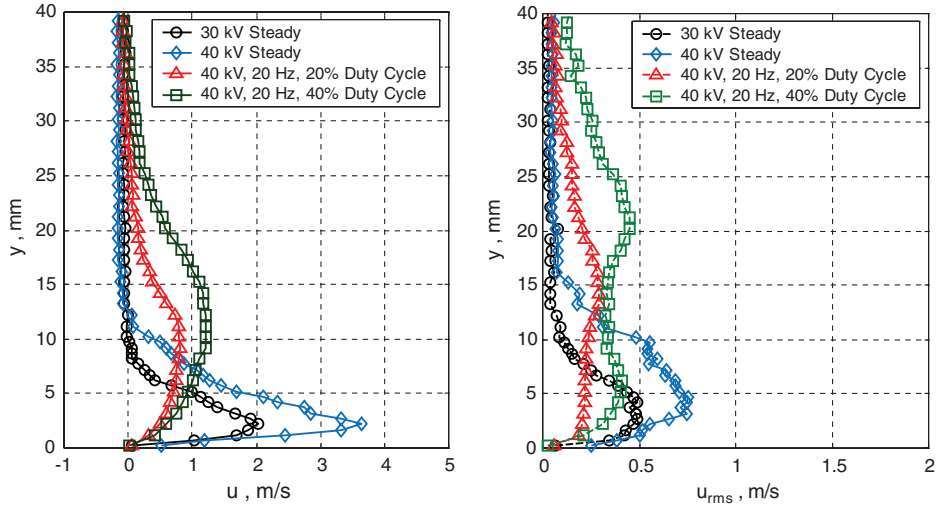

Fig. 11 Velocity profiles measured with LDV 75 mm downstream of a spanwise actuator operated in ambient air for steady and unsteady actuation: a) mean, and b) rms.

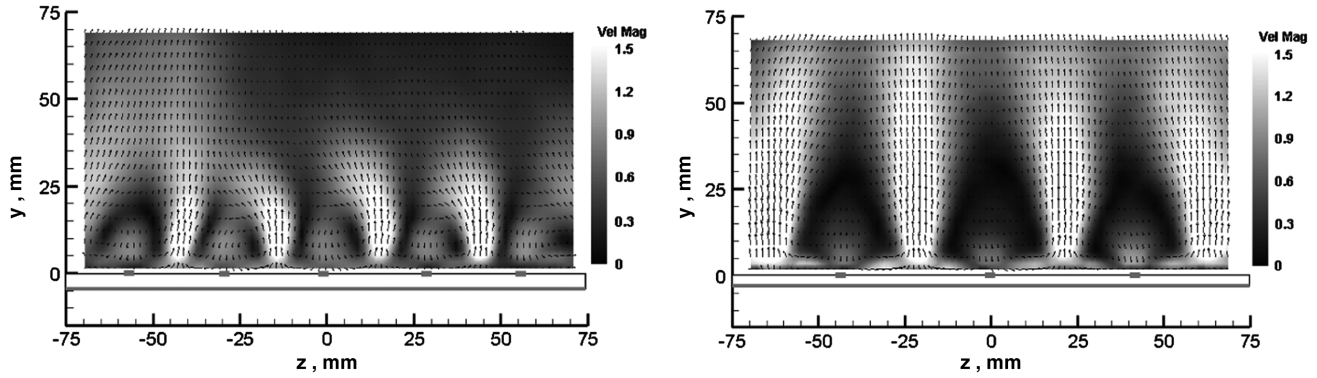

Fig. 12 Induced velocity field [m/s] in ambient air for PSVG actuator with a) $z = 25$ mm b) $z = 38$ mm.

C. Separation Control

Plasma actuators were used for separation control of the turbulent boundary layer over the convex ramp section. Flow visualization, two-component PIV, one-component LDV, and surface pressure measurements were used to characterize and compare the different actuation strategies. Smoke visualization was performed by introducing a continuous smoke streak upstream of the wind-tunnel inlet. An argon-ion laser light sheet illuminated the centerplane of the smoke that filled the turbulent boundary layer. A FASTCAM-ultima APX high-speed video camera system was used to record the smoke visualization. This flow visualization technique allowed for videos of the separation control at 4000 frames per second. This frame rate is 21.7 times faster than the characteristic time scale of the boundary layer δ/U_∞, where the boundary-layer thickness is measured at the beginning of the ramp section. Boundary-layer measurements were conducted by traversing the LDV probe volume locally normal to the ramp surface to measure the streamwise velocity profiles for the different actuation strategies.

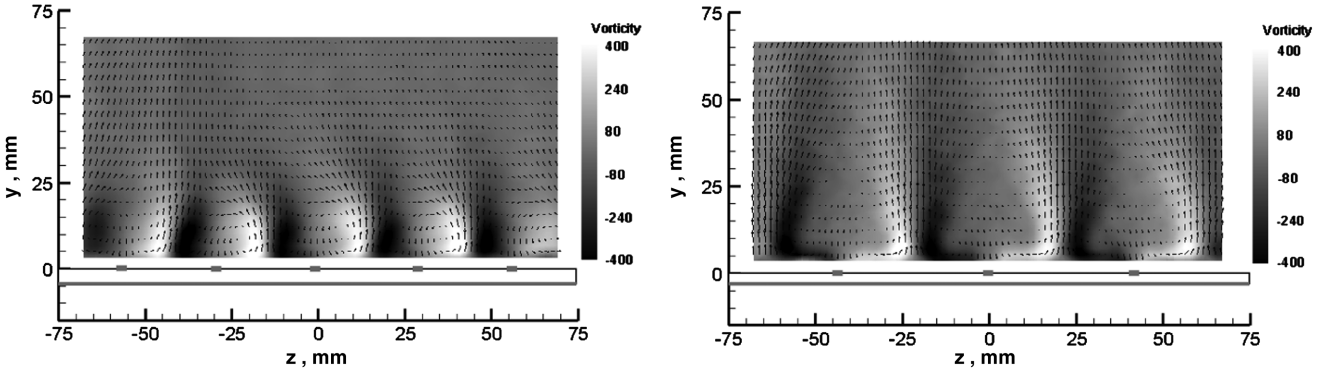

Fig. 13 Induced vorticity field (s^{-1}) in ambient air for PSVG actuator with a) $z = 25$ mm, and b) $z = 38$ mm.

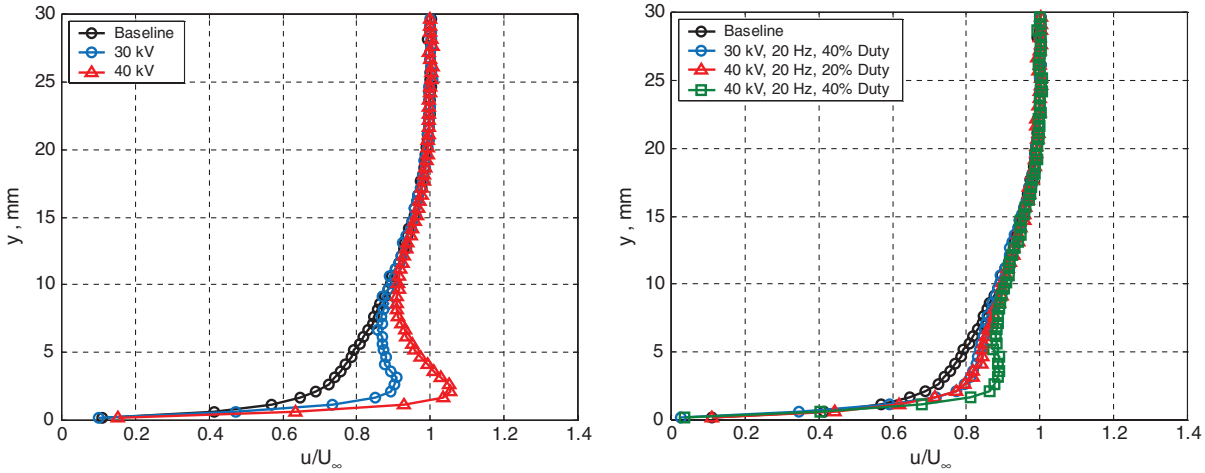

a) b)

Fig. 14 Boundary-layer profiles over flat plate for a) steady and b) unsteady actuation.

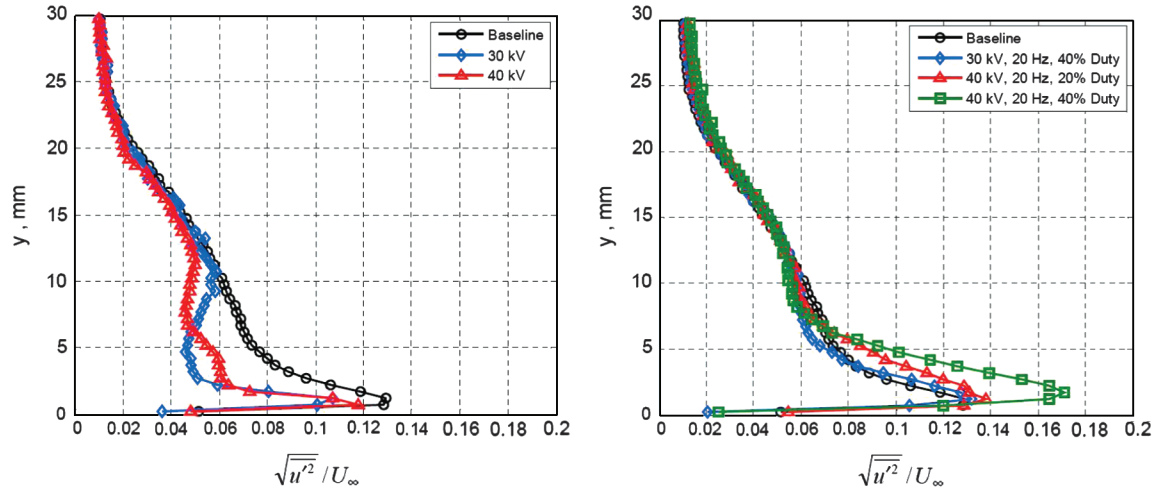

a) b)

Fig. 15 Turbulence intensity profiles over flat plate for a) steady and b) unsteady actuation.

1. Spanwise Steady Actuation

Steady spanwise actuation reattached the separated turbulent boundary layer. Figure 16a shows an image of the plasma-off case in which a region of intermittent reverse flow is observed over a portion of the ramp section. The turbulent structures within the boundary layer are observed to thicken and subsequently lift off the ramp surface. Figure 17b shows the attached turbulent boundary layer for steady spanwise actuation with $V_{pp} = 40$ kV. The high-speed video shows the flow reattaches in less than 0.08 s (equivalent to $15\delta/U_\infty$) after plasma initiation. It is interesting to note that, to good approximation, this corresponds to the convective time scale for flow over the convex ramp surface. The high-speed video captures a downward-induced velocity immediately above the exposed electrode and a jetting along the ramp surface downstream of the actuator as illustrated schematically by the arrow in Fig. 16b.

The PIV measurement of the time-average global velocity field for the plasma-off case of flow over the 25° ramp section is shown in Fig. 17a. This shows the separated flow just downstream of the spanwise actuator placement. The corresponding vorticity field in Fig. 17b clearly shows the separated shear layer over the ramp surface. Figure 18a shows the time-average velocity field for spanwise actuation at $V_{pp} = 40$ kV and the flow reattached to the ramp surface, while Fig. 18b clearly shows that the steady actuation has eliminated the separated shear layer in the vorticity field. Because the boundary layer is attached, the vorticity is now concentrated primarily in the near wall region which is not resolved in Fig. 18b.

Table 1 Boundary-layer characteristics for profiles measured on flat plate at $\Delta x/\delta = 3.7$

Case	δ, mm	δ^*, mm	δ^*, % change from baseline	θ, mm	θ, % change from baseline	H
Plasma-off	20.2	3.2	——	2.1	——	1.50
Steady spanwise, 30 kV	19.9	2.4	−26%	1.7	−22%	1.42
Steady spanwise, 40 kV	19.2	1.4	−57%	0.9	−58%	1.51
Unsteady, 30 KV 40% duty cycle	20.1	2.9	−7.9%	1.9	−9.2%	1.52
Unsteady, 40 KV 20% duty cycle	20.3	2.7	−15%	1.9	−12%	1.45
Unsteady, 40 KV 40% duty cycle	19.8	2.4	−26%	1.6	−26%	1.50

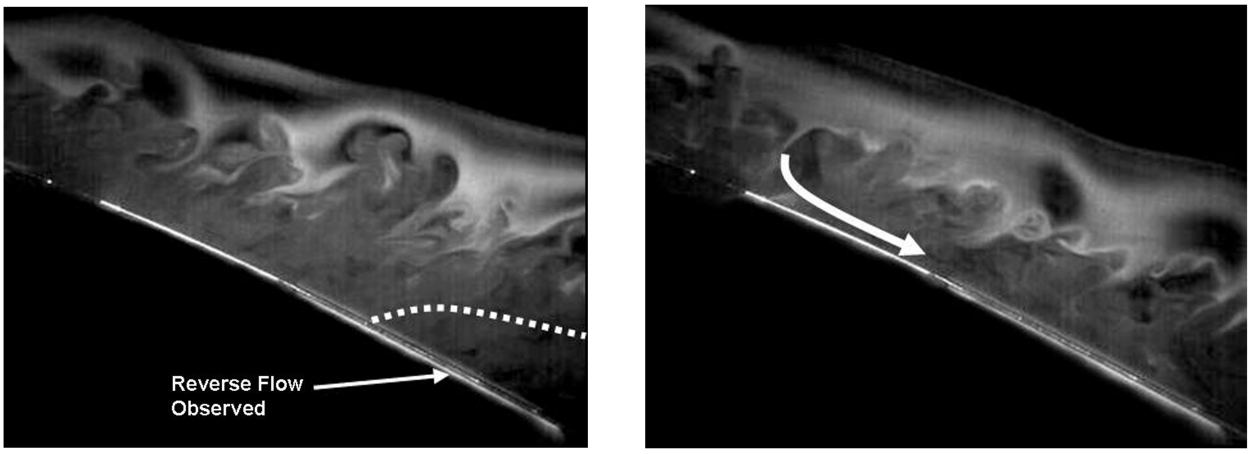

a) b)

Fig. 16 Smoke flow visualization of the spanwise steady actuation, $V_{pp} = 40$ kV: a) off, and b) on.

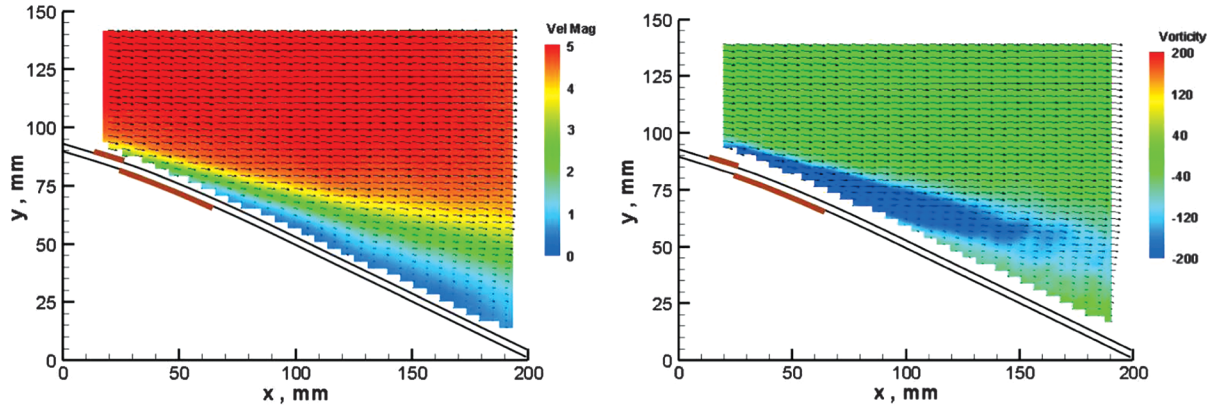

a) b)

Fig. 17 PIV measurements of the ramp section for the plasma-off case: a) velocity field (m/s), and b) vorticity.

The differential mean velocity field resulting from subtracting the plasma-off case from the steady spanwise actuation case is shown in Fig. 19. This shows a small downward velocity field above the actuator, and large near-wall momentum addition downstream of the actuator.

Streamwise mean velocity profiles were measured with the LDV system for the steady spanwise actuation cases and compared with the plasma-off case at the same streamwise locations. Figure 20 shows the mean velocity profiles measured normal to the ramp surface at two locations downstream of the actuator. For the plasma-off mean velocity profiles, the very small positive velocity near the wall is a consequence of intermittent flow reversal. The case of steady actuation at $V_{pp} = 40$ kV indicates momentum addition to the near-wall region, and the mean velocity profile shape is still developing at $\Delta x/\delta = 7.8$ downstream of the actuator. Boundary-layer characteristics were calculated for the profiles extracted at $\Delta x/\delta = 7.8$, including the velocity profile shape factor. For steady actuation at $V_{pp} = 40$ kV the shape factor is reduced from the plasma-off case of

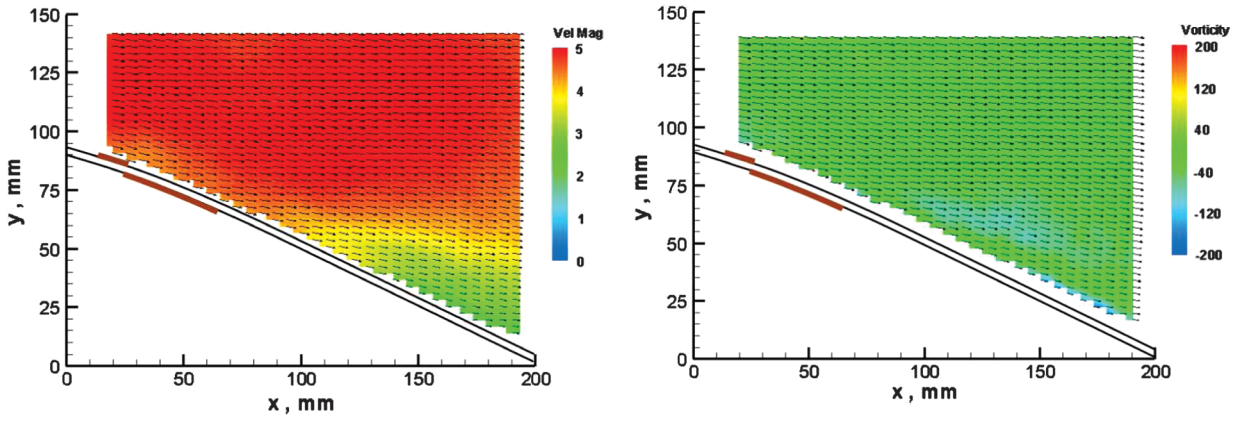

a) b)

Fig. 18 Spanwise steady actuation, $V_{pp} = 40$ kV: a) velocity field (m/s) and b) vorticity field.

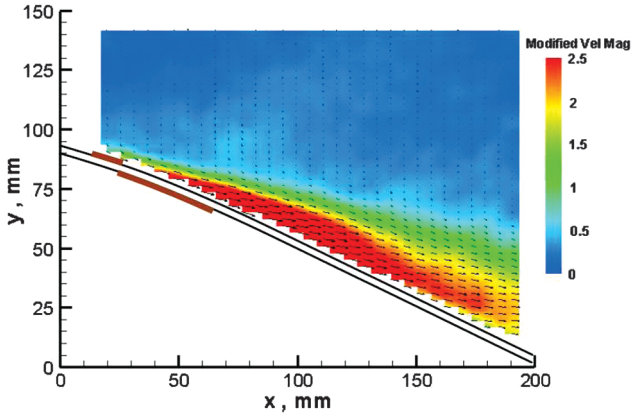

Fig. 19 Differential velocity field (m/s) of spanwise steady actuation, $V_{pp} = 40$ kV minus the plasma-off case.

$H = 3.03$ to $H = 1.51$. For steady actuation at a lower voltage of $V_{pp} = 30$ kV, the momentum addition was reduced with $H = 1.91$. Figure 21 shows the turbulence intensity profiles for steady actuation. As a result of the steady spanwise plasma actuation, the turbulence intensity was increased in the near wall region but reduced throughout most of the boundary layer, which is indicative of the elimination of the separated shear layer. Figure 22 shows a sample histogram of the LDV velocity measurements at $y_n = 2.5$ mm, and $\Delta x/\delta = 7.8$. The intermittent reversed flow observed in the plasma-off case has been entirely eliminated with steady plasma actuation at $V_{pp} = 40$ kV.

Surface pressure measurements were also used to evaluate the actuator effectiveness. Because of the high applied voltage used for plasma actuation, surface pressure measurements were not possible in the vicinity of the actuator. Pressure taps in the dielectric material would create an electrical path for the exposed electrode to arc to the covered electrode. Consequently, surface pressure measurements were only conducted on the downstream portion of the ramp section on the centerline of the end contour. Figure 23 shows the surface pressure distribution over the ramp section and end contour for steady spanwise actuation and a range of applied actuator voltages. As the voltage is increased, the pressure along the contour also increases. The integrated pressure over the length of the end contour was calculated for the steady actuation cases and compared with the plasma-off case. The percent increase in integrated ramp surface pressure coefficient as a function of applied actuator voltage shows a linear relationship over the voltage range in Fig. 24. It is noted that the integrated pressure coefficient is increased by 53% at the maximum actuator voltage employed. This qualitative metric serves to provide a measure of the relative degree of flow attachment provided by the plasma actuators.

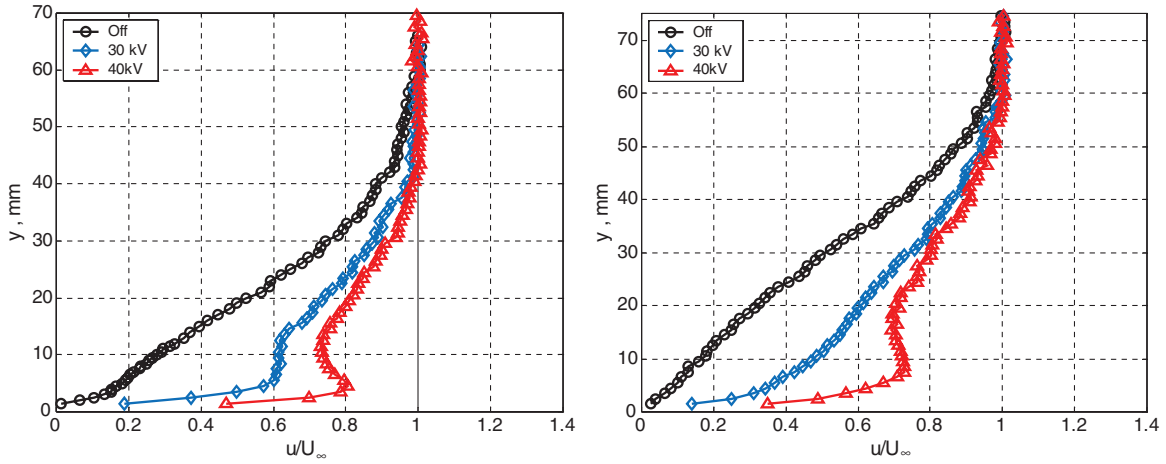

Fig. 20 Velocity profiles measured with LDV for steady spanwise actuation at a) $\Delta x/\delta = 4.8$, and b) $\Delta x/\delta = 7.8$.

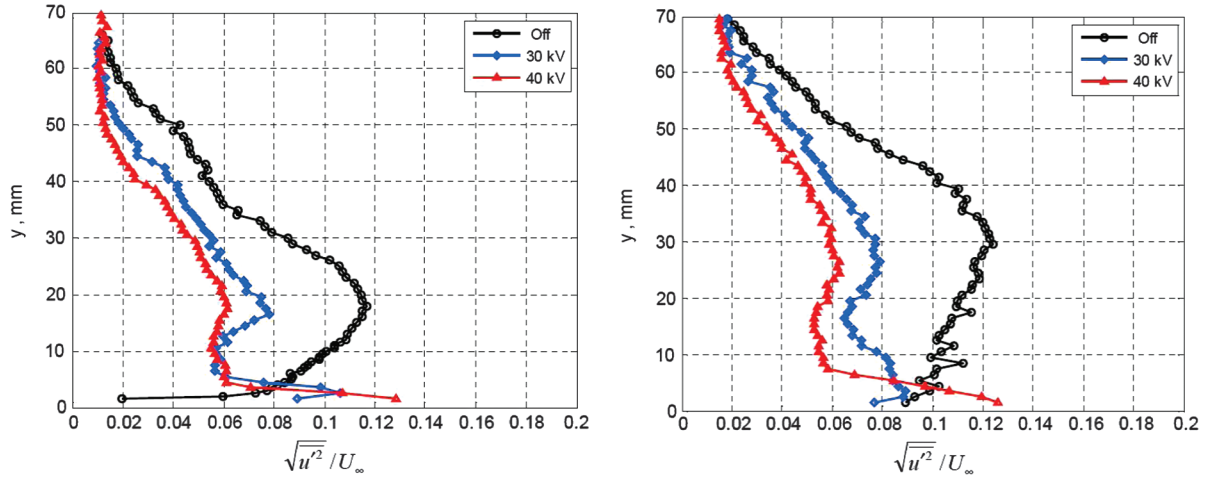

Fig. 21 Turbulence intensity profiles measured with LDV for steady spanwise actuation at a) $\Delta x/\delta = 4.8$, and b) $\Delta x/\delta = 7.8$.

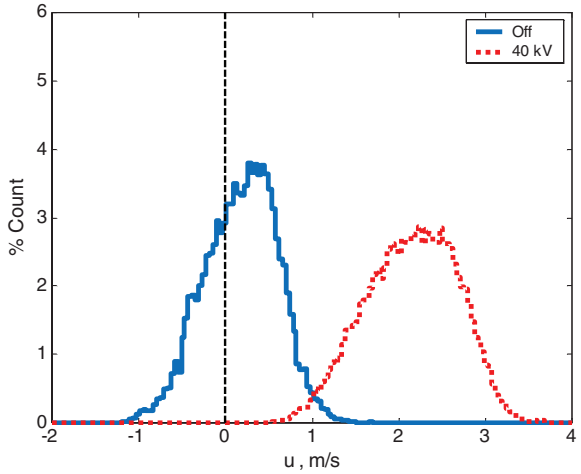

Fig. 22 Histogram of LDV velocity measurements at $\Delta x/\delta = 7.8$ and $y = 2.5$ mm for plasma-off and steady spanwise actuation, $V_{pp} = 40$ kV.

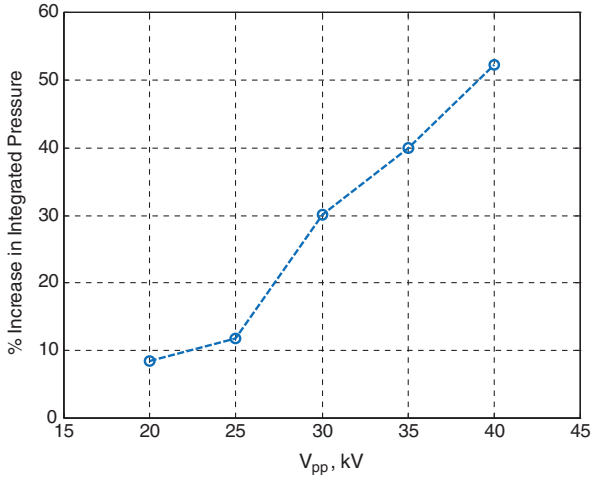

Fig. 24 Percent increase in the integrated surface pressure over the end contour as a function of applied voltage for steady spanwise actuation.

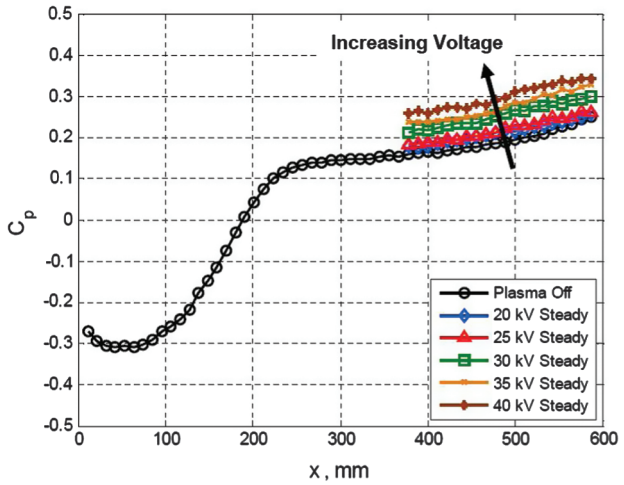

Fig. 23 Surface pressure distribution over ramp section and end contour for steady spanwise actuation.

2. Spanwise Unsteady Actuation

The effectiveness of unsteady spanwise actuation for turbulent boundary-layer separation control was also investigated. Unsteady actuation frequencies covering a reduced frequency range of $F^+ = 0.9$–8.6 were explored, where $F^+ \equiv fx_s/U_\infty$, and x_s is the streamwise length from the actuator to the end of the ramp section. It is widely recognized that $F^+ \approx 1$ is often optimum in terms of unsteady separation control if the characteristic length is based on the extent of the separated flow region. The frequency sweep investigated in this study showed little variation in actuator effectiveness. For the unsteady spanwise actuation results presented in the section, the actuation frequency was fixed at either $f = 20$ Hz or $f = 40$ Hz, which corresponds to $F^+ \approx 0.9$ and 1.8, respectively. These results may be considered representative.

Figure 25a shows the velocity field with spanwise actuation for $V_{pp} = 40$ kV, $f = 20$ Hz, and a duty cycle of 40%. The unsteady actuation successfully reattached the flow to the ramp section, and the corresponding vorticity field in Fig. 25b shows that the separated shear layer has been eliminated. Figure 26 shows the velocity profiles measured for unsteady spanwise actuation with $V_{pp} = 40$ kV and $f = 20$ Hz. The mean profile measured at $\Delta x/\delta = 7.8$ shows that unsteady actuation with a 40% duty cycle reduces the shape factor to $H = 1.95$. A reduction in duty cycle to 20% resulted in a reduction in momentum addition to the boundary layer with $H = 2.30$. Figure 27 shows the streamwise-component turbulence intensity profiles and the elimination of the separated shear layer due to the unsteady actuation. Peak turbulence intensity occurs farther away from the wall when compared with the steady actuation case due to the injection of spanwise vortices into the boundary layer.

The surface pressure distribution over the end contour was integrated for unsteady spanwise actuation at $V_{pp} = 40$ kV and $f = 40$ Hz over a range of duty cycles. Figure 28 shows that the percent increase in integrated pressure increased approximately linearly as a function of duty cycle. With the applied voltage fixed to 40 kV and a constant duty cycle of 40%, the actuator effectiveness as

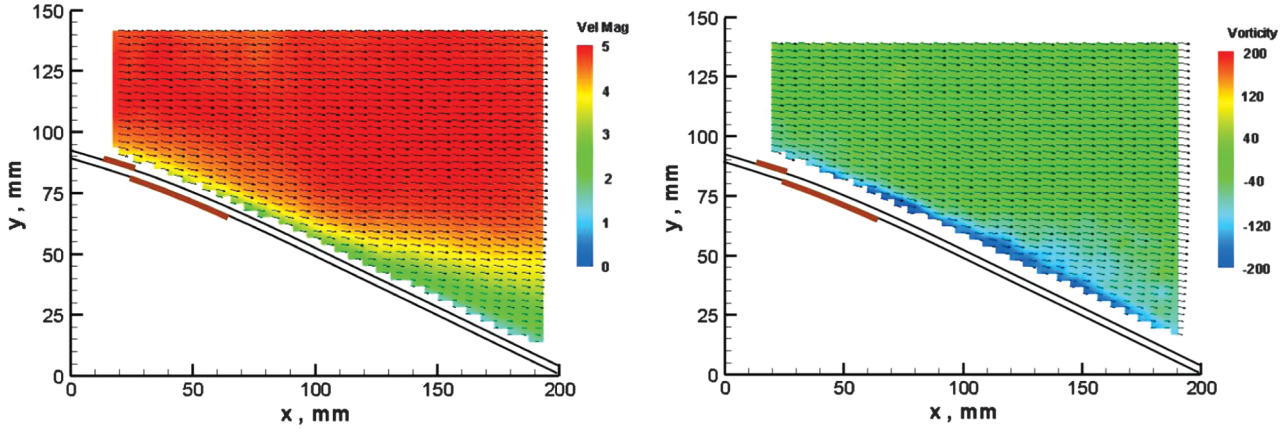

a) b)

Fig. 25 Spanwise unsteady actuation, $V_{pp} = 40$ kV, $f = 20$ Hz, 40% duty cycle: a) velocity field (m/s), and b) vorticity field.

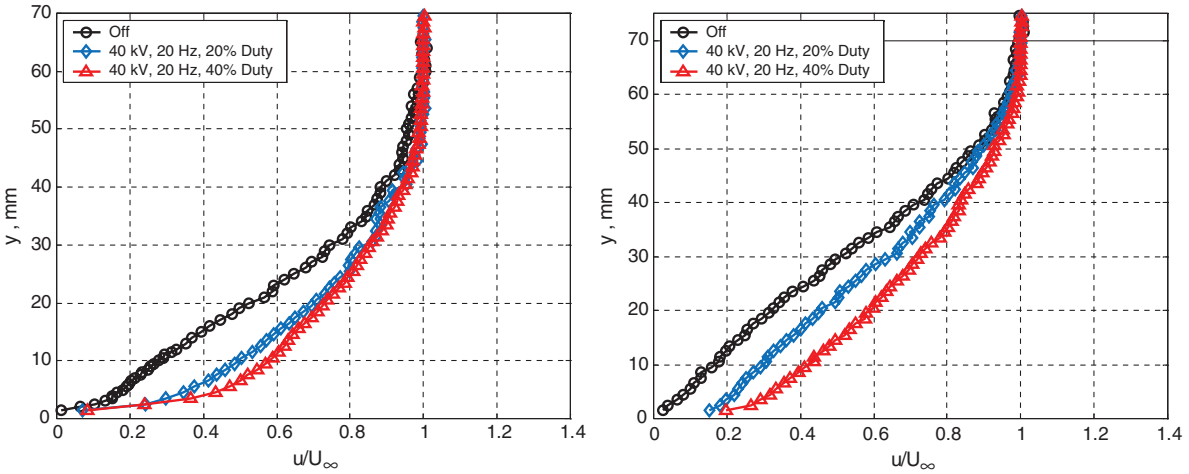

Fig. 26 Velocity profiles measured with LDV for unsteady spanwise actuation at a) $\Delta x/\delta = 4.8$, and b) $\Delta x/\delta = 7.8$.

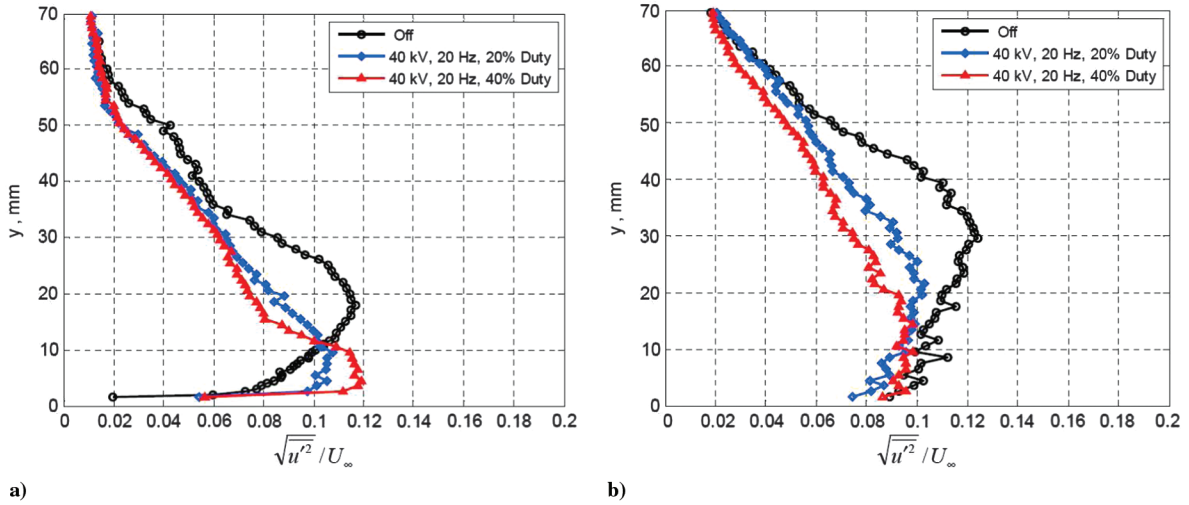

Fig. 27 Turbulence intensity profiles measured with LDV for unsteady spanwise actuation at a) $\Delta x/\delta = 4.8$, and b) $\Delta x/\delta = 7.8$.

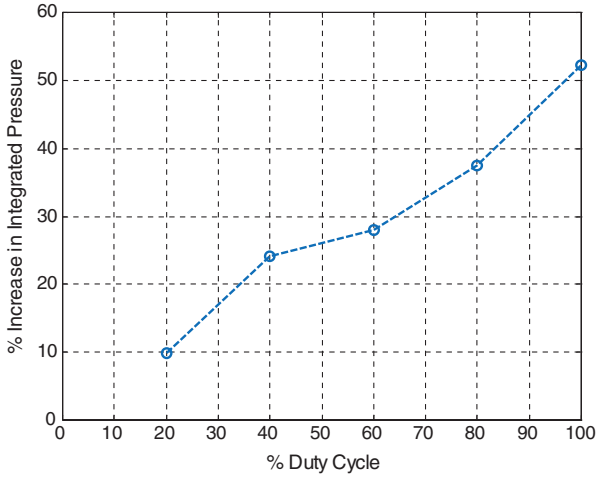

Fig. 28 Percent increase in the integrated surface pressure coefficient over the end contour as a function of duty cycle for unsteady spanwise actuation.

characterized by integrated pressure showed little sensitivity to the aforementioned range of unsteady actuation frequency.

3. *PSVG Actuation*

The PSVG actuators as shown in Fig. 8b with 38 mm spacing ($z/\delta = 1.4$) were also used to control the turbulent boundary-layer separation on the ramp section. Figure 12 shows that the spanwise-induced velocity field in ambient air produced a downward velocity over the exposed electrodes and a strong upward jet between a pair of adjacent electrodes. This PSVG actuation process in the ramp boundary layer was captured using the high-speed flow visualization technique by using the laser light sheet to illuminate a plane above the center exposed electrode, and a plane centered between two adjacent exposed electrodes of the PSVG actuator. The high-speed video showed that the PSVG actuator at $V_{pp} = 40$ kV reattached the flow in less than 0.085 s ($16\delta/U_\infty$) from plasma initiation. This is approximately the convective time scale for flow over the ramp section.

The video with the laser light sheet over the exposed electrode showed that the plasma caused a downward velocity to be directed toward the ramp surface downstream of the PSVG actuator. Figure 29a shows a frame of the attached flow from the smoke visualization high-speed video for this case. Figure 29b shows the smoke visualization with the laser light sheet centered between two electrodes. Note the turbulent structures of the outer layer are farther

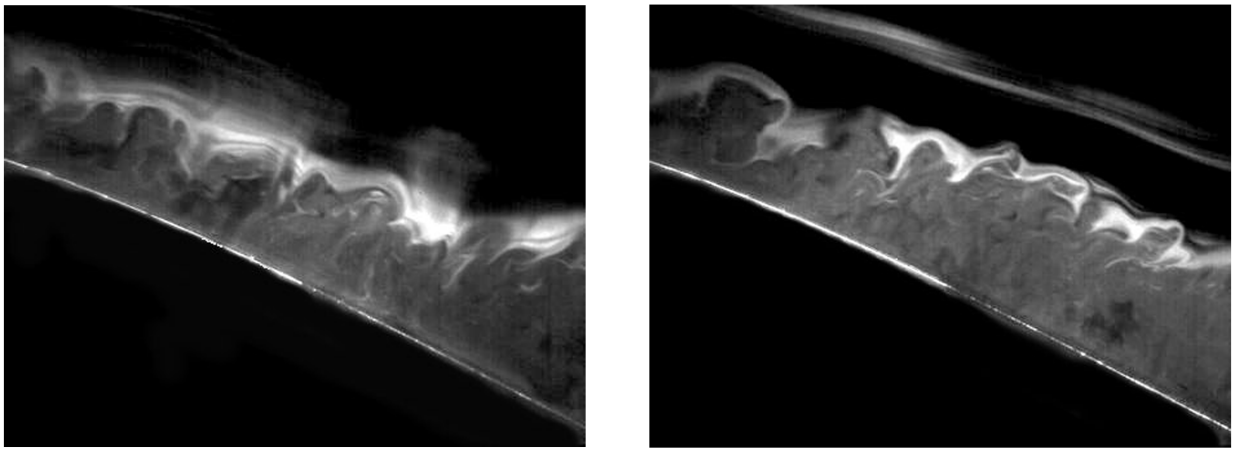

a) b)

Fig. 29 Smoke visualization over ramp section for PSVG with 38 mm spacing, $V_{pp} = 40$ kV, light sheet: a) over center electrode, and b) between adjacent electrodes.

away from the wall than in Fig. 29a. The high-speed video for this case showed an upward induced velocity within the turbulent boundary layer. This upward velocity is restricted to the internal turbulent boundary-layer structures and does not influence the potential flow outside the boundary layer. The upward and downward motion in planes separated by 19 mm is indicative of the formation of counter-rotating streamwise vortices within the boundary layer. This leads to enhanced mixing of momentum in the boundary layer and prevents separation from the ramp surface.

PIV measurements of the PSVG actuation confirm the qualitative observations from the high-speed smoke flow visualization. The mean velocity field for the plane above the center exposed electrode of the PSVG actuator is shown in Fig. 30a for $V_{pp} = 40$ kV, and the velocity field centered between exposed electrodes is shown in

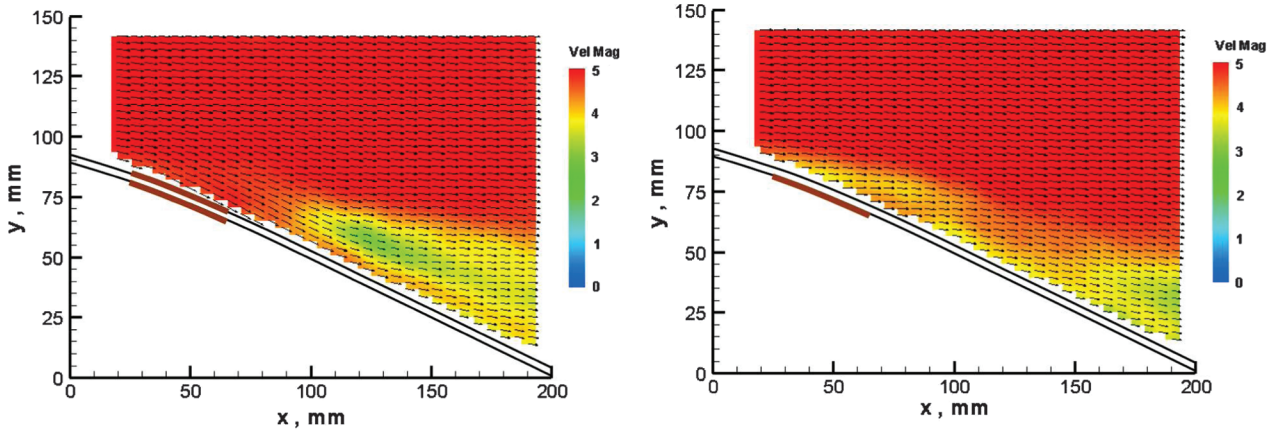

a) b)

Fig. 30 Velocity field (m/s) over ramp section for PSVG with 38 mm spacing, $V_{pp} = 40$ kV, measurement plane: a) over center electrode, and b) between adjacent electrodes.

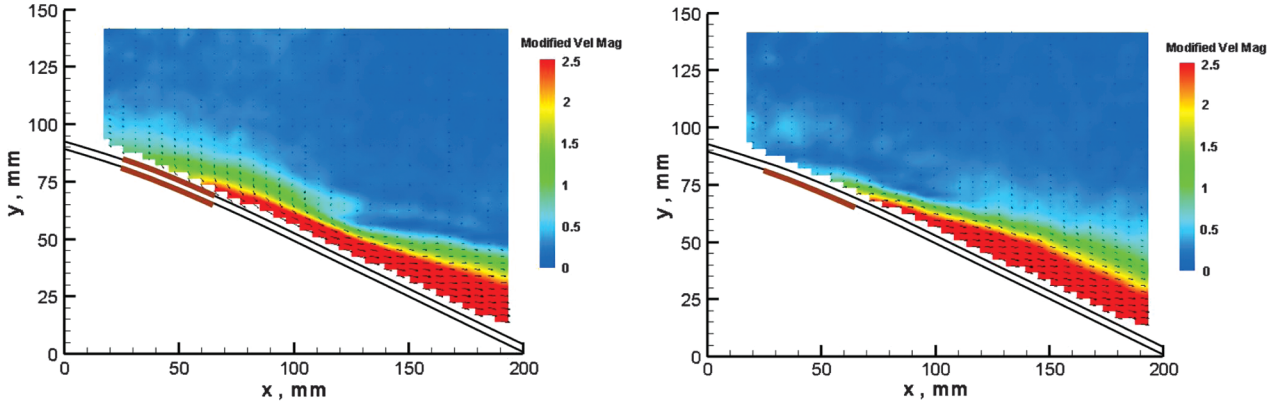

a) b)

Fig. 31 Velocity field (m/s) minus baseline case over ramp section for PSVG with 38 mm spacing, $V_{pp} = 40$ kV, measurement plane: a) over center electrode, and b) between adjacent electrodes.

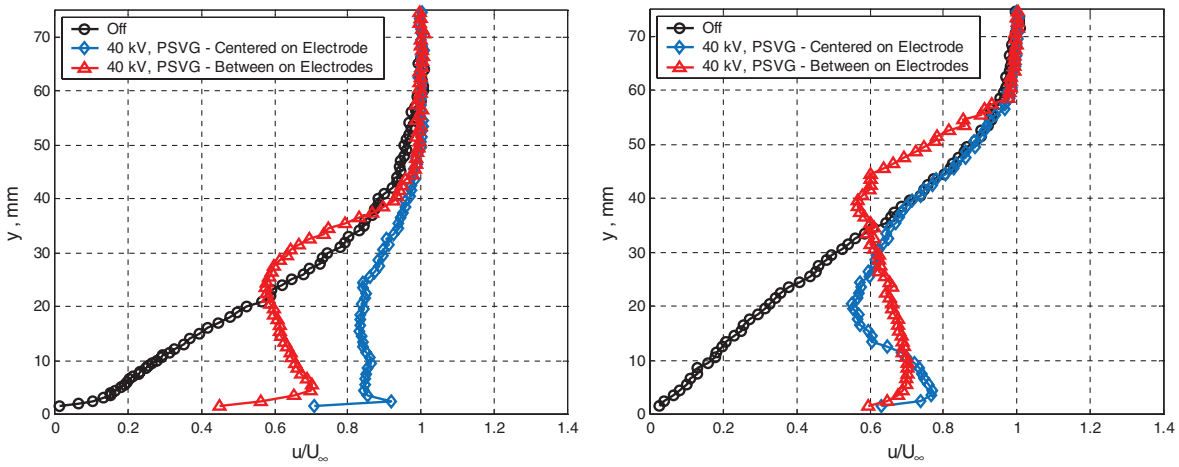

Fig. 32 Velocity profiles measured with LDV for PSVG actuation at a) $\Delta x/\delta = 4.8$, and b) $\Delta x/\delta = 7.8$.

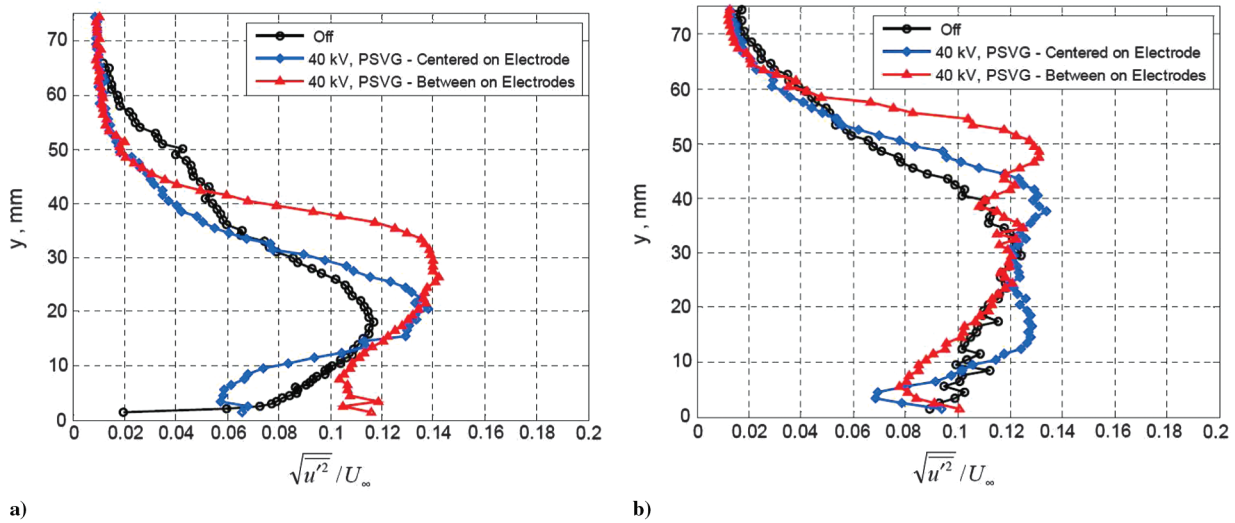

Fig. 33 Turbulence intensity profiles measured with LDV for PSVG actuation at a) $\Delta x/\delta = 4.8$, and b) $\Delta x/\delta = 7.8$.

Fig. 30b. The differential velocity fields for each PSVG actuation case minus the plasma-off case are shown in Fig. 31. The measurement plane above the center exposed electrode in Fig. 31a shows a differential velocity field directed downward toward the ramp surface. The measurement plane centered between adjacent exposed electrodes of the PSVG actuator in Fig. 31b shows a differential mean velocity field directed upward just downstream of the actuator. This is consistent with the ambient air PIV measurements and the high-speed smoke flow visualization videos of the PSVG separation control.

Mean velocity profiles measured with the LDV system for the PSVG actuation are shown in Fig. 32. The profiles measured with the probe volume centered over the exposed electrode show momentum addition to the near wall region. Evaluation of the boundary-layer characteristics for the profile measured downstream of the actuator at $\Delta x/\delta = 7.8$ shows that $H = 1.57$. The profiles measured with the probe volume centered between adjacent electrodes show momentum addition away from the wall, and $H = 1.58$. It is clear that the mean velocity profiles due to PSVG actuation are still evolving at $\Delta x/\delta = 7.8$. That is, large-scale cross-stream mixing of momentum is still occurring. The corresponding streamwise-component turbulence intensity profiles in Fig. 33 show that for each PSVG actuation case the turbulence intensity is increased near the outer portion of the boundary layer. This is indicative of increased mixing of momentum due to the production of streamwise vorticity. A summary of the boundary-layer characteristics for each ramp actuation case is shown Table 2.

The surface pressure distribution over the end contour was integrated for PSVG actuation with $z = 38$ mm and over a range of applied voltage. Figure 34 shows that the percent increase in integrated pressure coefficient increases approximately linearly with increasing voltage up to the maximum applied voltage of 40 kV.

Figure 35 compares the percent increase in integrated pressure as a function of actuator power consumption per meter span of covered electrode for steady, unsteady, and PSVG actuation. The steady spanwise actuation results represent a voltage range of 20–40 kV. The unsteady actuation results are for a fixed voltage of 40 kV and a duty cycle range of 20–100%. The PSVG results are for $z = 38$ mm, and a range of applied voltage of 15–40 kV. The actuator effectiveness increases as the power increases for each actuation strategy. Even though each actuation strategy uses distinctly different

Table 2 Boundary-layer characteristics for profiles measured at $\Delta x/\delta = 7.8$

Case	δ, mm	δ^*, mm	θ, mm	H
Plasma-off	69.1	29.4	9.68	3.03
Steady spanwise, 30 kV	58.0	17.9	9.37	1.91
Steady spanwise, 40 kV	55.2	12.0	7.96	1.51
Unsteady, 40 KV 20% duty cycle	63.3	23.9	10.40	2.30
Unsteady, 40 KV 40% duty cycle	59.5	19.0	9.72	1.95
PSVG, 40 kV, over electrode	63.6	17.2	10.96	1.57
PSVG, 40 kV, between electrodes	63.4	19.4	12.27	1.58

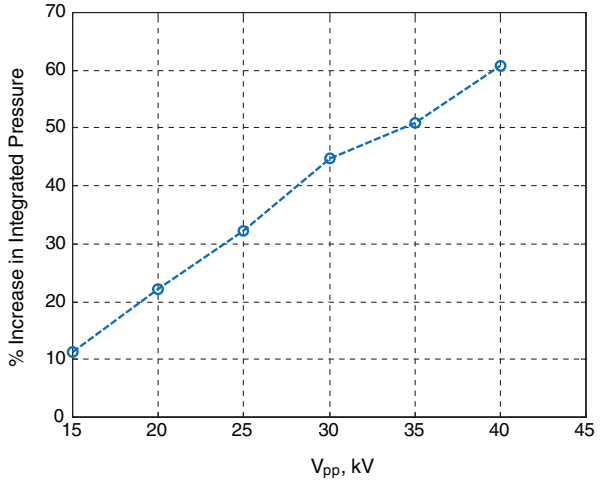

Fig. 34 Percent increase in the integrated surface pressure over the end contour as a function of applied voltage for PSVG actuation.

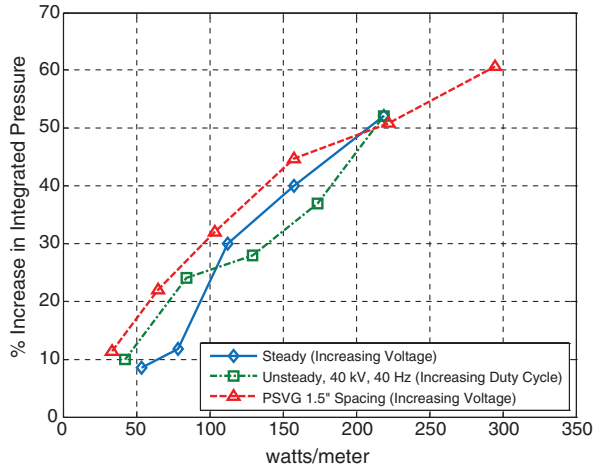

Fig. 35 Percent increase in the integrated surface pressure over the end contour as a function of power per unit span of covered electrode for each actuation strategy.

physical mechanisms for flow control, each appears to exhibit comparable efficiency in terms of integrated ramp pressure increase per power input (per unit span of covered electrode).

IV. Conclusions

The results of the plasma flow control experiments presented in this paper demonstrate the use of SDBD plasma actuators for APG turbulent boundary-layer separation control. In the absence of an external flow, PIV measurements show that steady spanwise actuation produced a thin wall jet while unsteady pulsed actuation produced a wider time-average velocity profile due to the creation of spanwise vortices that propagate downstream and away from the wall. The PSVG actuators induced a velocity field that produced regions of counter-rotating streamwise vorticity over the span of the actuator. The nature of the induced PSVG velocity field is dependent on the spacing z between adjacent exposed electrodes, and the regions of counter-rotating vorticity are separated by a distance of approximately $z/2$.

Experimental results demonstrate near-wall momentum addition due to both steady and pulsed/unsteady spanwise plasma actuation on an attached ZPG turbulent boundary layer over a flat plate. Both methods of actuation had the effect of significantly reducing both the integral displacement and momentum thickness. By comparison, the effect on the boundary-layer thickness was small. For steady actuation the streamwise-component turbulence intensity in the boundary layer is reduced from that observed in the natural flow. In contrast, unsteady actuation resulted in increased streamwise-component turbulence intensity in the boundary layer due to the formation of unsteady spanwise vortices.

Plasma actuators were also used to control APG turbulent boundary-layer separation from a convex ramp. The spanwise actuator located just upstream of the separation location reattached the separated flow. Flow visualization, PIV, and LDV measurements indicate that momentum addition to the near-wall region associated with a steady plasma-induced wall jet resulted in boundary-layer reattachment. Downstream ramp surface pressure measurements showed that the actuator effectiveness increased with applied actuator voltage. Integrated ramp surface pressure coefficient increased by 53% with steady plasma actuation at 40 kV_{p-p} (the largest applied voltage used in this study). Unsteady spanwise plasma actuation also reattached the separated ramp flow. However, the unsteady spanwise actuation showed little sensitivity to the unsteady frequency used (over the rather large reduced frequency range of $F^+ = 0.9$–8.6). This lack of sensitivity to unsteady frequency suggests the plasma actuation did not exploit a flow instability as is often the case in laminar separation control applications. If instabilities are not exploited then the only thing that matters in terms of avoiding separation is the amount of high momentum fluid that is transferred to the near-wall region. This would increase with duty cycle for the unsteady spanwise actuation case. Figure 28 confirms that the effectiveness of unsteady plasma flow control increases with the duty cycle. Similarly, for steady spanwise actuation, Fig. 24 shows that the effectiveness of plasma flow control increases with applied voltage (the magnitude of the applied body force).

The PSVG actuators were also quite successful in reattaching the turbulent boundary layer over the convex ramp section. The flow visualization and the PIV measurements showed a downward induced velocity in the measurement plane over the exposed electrode, and an upward induced velocity in the plane centered between adjacent electrodes. This motion embedded within the turbulent boundary layer is indicative of counter-rotating streamwise vortices. These serve to augment cross-stream momentum transfer that serves to reattach the flow. The mean velocity profiles measured with PSVG suggest more rapid mixing than for steady or unsteady spanwise actuation cases. Integrated ramp surface pressure measurements indicate a 60% increase in ramp surface pressure coefficient at the maximum applied voltage of 40 kV_{p-p}.

For each type of plasma flow control investigated, separation control depends critically on augmenting momentum transfer to the near-wall region. The maximum excitation voltage applied in this study was 40 kV_{p-p}. Higher applied voltages gave rise to streamer formation and actuator saturation. To apply higher actuator voltages, and thereby further increase near-wall momentum transfer, the actuators would need to be modified in terms of their dielectric thickness and/or material as described in [17]. This would allow APG turbulent boundary-layer separation control at higher Reynolds numbers.

Acknowledgments

This work was supported in part by Bell Helicopter and monitored by Tom Wood and by the U.S. Army Research Office under W911NF-07-1-0122 and monitored by Tom Doligalski. The authors gratefully acknowledge this support.

References

[1] Gad-El-Hak, M., and Bushnell, D. M., "Separation Control: A Review," *Journal of Fluids Engineering*, Vol. 113, No. 1, 1991, pp. 5–30. doi:10.1115/1.2926497

[2] Seifert, A., Greenblatt, D., and Wygnanski, I. J., "Active Separation Control: An Overview of Reynolds and Mach Number Effects," *Aerospace Science and Technology*, Vol. 8, No. 7, 2004, pp. 569–582. doi:10.1016/j.ast.2004.06.007

[3] Amitay, M., Smith, D. R., Kibens, V., Parekh, D. E., and Glezer, A., "Aerodynamics Flow Control Over and Unconventional Airfoil Using Synthetic Jet Actuators," *AIAA Journal*, Vol. 39, No. 3, 2001, pp. 361–370.

doi:10.2514/2.1323
[4] Amitay, M., Smith, D. R., and Glezer, A., "Aerodynamic Flow Control Using Synthetic Jet Technology," AIAA Paper 98-0208, 1998.
[5] Corke, T. C., Post, M. L., and Orlov, D. M., "Single Dielectric Barrier Discharge Plasma Enhanced Aerodynamics: Physics, Modeling and Applications," *Experiments in Fluids*, Vol. 46, No. 1, 2009, pp. 1–26. doi:10.1007/s00348-008-0582-5
[6] Post, M. L., and Corke, T. C., "Separation Control on High Angle of Attack Airfoil Using Plasma Actuators," *AIAA Journal*, Vol. 42, No. 11, 2004, pp. 2177–2184. doi:10.2514/1.2929
[7] Post, M. L., and Corke, T. C., "Separation Control Using Plasma Actuators: Dynamic Stall Vortex Control on Oscillating Airfoil," *AIAA Journal*, Vol. 44, No. 12, 2006, pp. 3125–3135. doi:10.2514/1.22716
[8] Thomas, F. O., Kozlov, A., and Corke, T. C., "Plasma Actuators for Bluff Body Flow Control," AIAA Paper 2006-2845, 2006.
[9] Thomas, F. O., Kozlov, A., and Corke, T. C., "Plasma Actuators for Landing Gear Noise Reduction," AIAA Paper 2005-3010, 2005.
[10] Thomas, F. O., Kozlov, A., and Corke, T. C., "Plasma Actuators for Cylinder Flow Control and Noise Reduction," *AIAA Journal*, Vol. 46, No. 8, 2008, pp. 1921–1931. doi:10.2514/1.27821
[11] Enloe, C. L., McLaughlin, T. E., VanDyken, R. D., Kachner, K. D., Jumper, E. J., and Corke, T. C., "Mechanisms and Responses of a Single Dielectric Barrier Plasma Actuator: Plasma Morphology," *AIAA Journal*, Vol. 42, No. 3, 2004, pp. 589–594. doi:10.2514/1.2305
[12] Enloe, C. L., McLaughlin, T. E., VanDyken, R. D., Kachner, K. D., Jumper, E. J., Corke, T. C., Post, M., and Haddad, O., "Mechanisms and Responses of a Single Dielectric Barrier Plasma Actuator: Geometric Effects," *AIAA Journal*, Vol. 42, No. 3, 2004, pp. 595–604. doi:10.2514/1.3884
[13] Post, M. L., "Phased plasma actuators for unsteady flow control," M.S. Thesis, Univ. of Notre Dame, 2001.
[14] He, C., and Corke, T. C., "Numerical and Experimental Analysis of Plasma Flow Control Over a Hump Model," AIAA Paper 2007-0935, 2007.
[15] Moreau, E., "Airflow control by Non-Thermal Plasma Actuators," *Journal of Physics D: Applied Physics*, Vol. 40, No. 3, 2007, pp. 605–636. doi:10.1088/0022-3727/40/3/S01
[16] Forte, M., Jolibois, J., Moreau, E., Touchard, G., and Cazalens, M., "Optimization of a Dielectric Barrier Discharge Actuator by Stationary and Non-Stationary Measurements of the Induced Flow Velocity: Application to Airflow Control," AIAA Paper 2006-2863, 2006.
[17] Thomas, F., Corke, T. C., Iqbal, M., Kozlov, A., and Schatzman, D., "Optimization of SDBD Plasma Actuators for Active Aerodynamic Flow Control," *AIAA Journal*, Vol. 47, No. 9, 2009, pp. 2169–2178. doi:10.2514/1.41588
[18] Orlov, D. M., "Modeling and Simulation of Single Dielectric Barrier Discharge Plasma Actuators," Ph.D. Dissertation, Univ. of Notre Dame, 2006.
[19] Huang, J., Corke, T., and Thomas, F., "Plasma Actuators for Separation Control of Low Pressure Turbine Blades," *AIAA Journal*, Vol. 44, No. 1, 2006, pp. 51–57. doi:10.2514/1.2903
[20] Huang, J., Corke, T., and Thomas, F., "Unsteady Plasma actuators for Separation Control of Low Pressure Turbine Blades," *AIAA Journal*, Vol. 44, No. 7, 2006, pp. 1477–1487. doi:10.2514/1.19243
[21] Goksel, B., Greenblatt, D., Rechenberg, I., Nayeri, C. N., and Paschereit, C. O., "Steady and Unsteady Plasma Wall Jets for Separation and Circulation Control," AIAA Paper 2006-3686, 2006.
[22] Greenblatt, D., Goksel, B., Rechenberg, I., Schule, C. Y., Romann, D., and Paschereit, C. O., "Dielectric Barrier Discharge Flow Control at Very Low Flight Reynolds Numbers," *AIAA Journal*, Vol. 46, No. 6, 2008, pp. 1528–1541. doi:10.2514/1.33388
[23] Klebanoff, P. S., "Characteristics of Turbulence in a Boundary Layer with Zero Pressure Gradient," NACA TR-1247, 1955.
[24] Schatzman, D., and Thomas, F., "Turbulent Boundary Layer Separation Control with Plasma Actuators," AIAA Paper 2008-4199, 2008.

A. Naguib
Associate Editor